Communication

A molecular dynamics study concerning the effect of high-temperature and high-pressure on the structure and phase transition of Fe$_2$O$_3$ material

Dung Nguyen Trong[1,2,*], Van Cao Long[1], Phu Nguyen Dang[3] and Ştefan Ţălu[4]

[1] Institute of Physics, University of Zielona Góra, Zielona Góra, Poland
[2] Faculty of Physics, Hanoi National University of Education, Hanoi, Vietnam
[3] Faculty of Electronics and Telecommunications, VNU-University of Engineering and Technology Hanoi, Vietnam
[4] The Directorate of Research, Development and Innovation Management (DMCDI), Technical University of Cluj-Napoca, Cluj County, Romania

* **Correspondence:** Email: dungntdt2018@gmail.com.

Abstract: This paper uses Molecular Dynamics (MD) method to study the influence of high temperature (T) and high pressure (P) on the structure and phase transition of Fe$_2$O$_3$ materials. The results show that, when increasing the temperature from T = 300 K to T = 7000 K, P = 0.0 GPa, the size (1) of the Fe$_2$O$_3$ materials increases, the energy (E) increases, the length link (r) decreased, the number of structural units FeO$_4$, FeO$_5$ increased, and FeO$_6$ decreased. Similarly, as the pressure (P) is increased, from P = 0 GPa to P = 360 GPa at temperatures T, l decreases, E increases, r decreases, FeO$_4$ decreases and disappears, FeO$_5$ decreases, and FeO$_6$ increases at high P with P ≥ 150 GPa, FeO$_5$ disappeared at P ≥ 250 GPa and only FeO$_6$ appeared at T = 2300, 7000 K. In addition, when increasing T, P, the bond angle of Fe–O–Fe, O–Fe–O decreases, E increases, r decreases, l increases when T increases and l decreases when P increases, leading to the number of structural units FeO$_4$, FeO$_5$ increasing and FeO$_6$ decreasing when T increases and vice versa when P increases. In addition, the phase transition temperature (T$_m$), T$_m$ = 2300 K was determined. All the obtained results will be the basis for future experimental studies of amorphous Fe$_2$O$_3$ materials.

Keywords: Fe$_2$O$_3$ materials; high temperature; high pressure; structure; molecular dynamics; simulation

1. Introduction

Fe$_2$O$_3$ material is the most common oxide material, very environmentally friendly and used in many fields of science and technology: Welding [1], magnetism [2], supercapacitor electrode [3], biomedicine [4], environment [5], ceramic materials [6–10], environmental contaminant removal [11], photocatalysis [12], chemical sensors [13], electrochemistry [14], magnetic resonance imaging, data storage [15–19], energy [20]. Energy with bandgap (E_g) of Fe$_2$O$_3$ materials with absorption range of 1.9–2.2 eV [21] that corresponds to half of the visible light region of wavelength (λ), $\lambda > 600$ µm, absorbing 40% of the sun's spectrum and this is a stable material in solutions with concentrations (pH), pH > 3.0 [22]. Fe$_2$O$_3$ exists in 5 allotropic states: α-Fe$_2$O$_3$ (hematite), β-Fe$_2$O$_3$ [23,24], γ-Fe$_2$O$_3$ (maghemite), ε-Fe$_2$O$_3$, [9,10,25] and ζ-Fe$_2$O$_3$ [25]. In literature, the polymorphic existence of amorphous Fe$_2$O$_3$ was investigated at temperature (T), T = 923 K [26–28]. Among them, ε-Fe$_2$O$_3$ was first identified in 1998 [29] and is considered a remarkable phase, with room temperature magnetic resonance T = 300 K [7,10,30] and is applied in the technology of making Jian ceramics of ancient China by heating clay containing Fe, T = ~1573 K [31]. While, at T = 923 K, Fe$_2$O$_3$ can be converted to Fe$_3$O$_4$ with the energy (E) that decreases very quickly [32–34]. On the other hand, the polymorphic phase transition from γ-Fe$_2$O$_3$ → ε-Fe$_2$O$_3$ → α-Fe$_2$O$_3$ has been studied in many previous works. The obtained results show that the material has a thermodynamically unstable structure [10,35]. Wheeler et al. [36] have successfully fabricated single-crystal Fe$_2$O$_3$ nanowires with high density, which have reduced the charge loss by electron-hole recombination. Also, it is known that the magnetic Curie temperature (T_c) of the ferrimagnet material is respectively T_c = 500/585 K [37–39]. To study and fabricate Fe$_2$O$_3$ materials based on the experimental methods [40,41], there are the following methods: X-ray diffraction (XRD), Extended X-ray Absorption Fine Structure (EXAFS) method [42], transmission electron microscopy, and High-Resolution Transmission Electron Microscopy (HRTEM) [43]. Schaetz et al. [44] have successfully determined the influence of nano-size, shape and surface elevation effect of nanomaterials on the structure of hematite (α-Fe$_2$O$_3$), and maghemite (γ-Fe$_2$O$_3$). In practical applications, Fe$_2$O$_3$ is also used in the separation of water by electrolysis of α-Fe$_2$O$_3$. Hematite electrodes can generate photons by illumination with a wavelength (λ), $\lambda = 350$ µm, without the need for a power source [45,46]. Fe$_2$O$_3$ thin films have been used in photovoltaic cells [47] with hematite nanorods (α-Fe$_2$O$_3$) with thicknesses from 5 nm to 7 nm with lengths from 3 nm to 4 nm [48]. In practical applications [49,50], when it is welded Fe$_2$O$_3$-doped Austenitic steel, better results are obtained than previous conventional methods, due to the self-reversing energy of Marangoni flow at the lower melting temperature of nanowire flux. Similarly, the practical applications of supercapacitor electrodes have also been solved by optimizing the structure of Fe$_2$O$_3$ nanotubes based on polyaniline (PANI) combination [3]. Besides, under the influence of Fe$_2$O$_3$, the positions of defects and oxygen-containing functional groups are improved significantly with band gap (E_g), $E_g < 2.8$ eV. Because of that, composites Fe$_2$O$_3$ are considered as materials that have visible light with photocatalysts and exhibit photocatalytic activity towards the degradation of cationic dye Rhodamine B (RhB) [12]. O. Iglesias and A. Labarta [51] applied the theoretical method (the Monte Carlo (MC) simulation method combined with periodic boundary conditions) to study the influence of the surface layer on the magnetic properties of nanomaterials at the temperature T = 350 K. VV Hoang and Khanh BTHL used the Molecular Dynamics (MD) method for the determination of the static and thermodynamic properties of liquid and amorphous Fe$_2$O$_3$ nanoparticles and concluded that with amorphous Fe$_2$O$_3$ nano, at T = 3500 K, the Fe–Fe, Fe–O, and O–O corresponding to links lengths

are $r_{Fe–Fe}$ = 3.1 Å, $r_{Fe–O}$ = 1.9 Å, $r_{O–O}$ = 2.7 Å [52]. In other studies, researchers found with the experimental method that Fe_2O_3 has $r_{Fe–Fe}$ = 3.35 Å, $r_{Fe–O}$ = 1.91/1.95 Å, $r_{O–O}$ = 2.91 Å [33,53] and $r_{Fe–O}$ = 2.08 Å [54]. Among these research methods, the MD simulation method is considered to have many advantages. With a simple method, just by the determination of the interaction between atoms by Newton's second law, together with the averaging statistics method, and applying the computational methods, it serves as a complement to conventional experiments. Based on these obtained results it can be concluded that the nanomaterials have a link length (r) always smaller than that of the bulk material. With the nanomaterials, no pick separation at the first pick of the Radial Distribution Function (RDF) can be observed. With amorphous material, the pick separation occurs at the first vertex of RDF and has 02 Picks, the first Pick has a link length of r_{11} = 3.11 Å and the second Pick has a link length of r_{12} = 3.40 Å [55] with link length $r_{Fe–Fe}$ = 3.11 Å related to octahedral link pair. Furthermore, the positions of Fe atoms are link to their edges and gradually increase to $r_{Fe–Fe}$ = 3.40 Å. Besides, the Coordination Number (CN) of nanomaterials increases when is increased the nano-size. The average coordination number (CN), $CN_{Fe–O}$ the range of 4.71–5.28, shows that α-Fe_2O_3, β-Fe_2O_3 tend to form an octahedral FeO_6 structure in the liquid state with T = 3500 K [54,56–58]. Similarly, the bond angle Fe–O–Fe of liquid Fe_2O_3 nanomaterials at T = 3500 K ranges from 83° to 99°. It is known that for the ideal FeO_6 configuration, the O–Fe–O angle is 90°, and for the ideal FeO_4 it is 109.5°. However, β-Fe_2O_3 and ε-Fe_2O_3 polymorphic structures with only superparamagnetic Fe_2O_3 nanomaterials [59] have octahedral structural units number of FeO_6, FeO_4 tetrahedra in ε-Fe_2O_3 [60–62]. The glass temperature (T_g) is an important parameter used for studies about amorphous materials. The glass temperature of Fe_2O_3 nanomaterials usually is calculated through the intersection of high linear temperature and low temperature extrapolated to the total energy. The values T_g = 2182.18 K, 1897.26 K, 1784.19 K, and 1610.33 K of nanomaterials correspond for the nano-size (D) (2, 3, 4, and 5 nm). Besides, there are also results showing that T_g increases with the increases of D [63,64]. For Fe_2O_3 materials, T_g = 1400 K has a much smaller value than nanomaterials. Based on the existing data it can be concluded that the results obtained are contradictory, and there are not yet results covering all types of materials such as nanomaterials, thin films, and bulk materials [63–66]. Besides, in some studies is also determined the phase transition temperature (T_m) [67]. It has been demonstrated that the obtained results depend on the specified research method and applied boundary conditions [66]. Well-documented studies highlighted that there are various factors such as the atomic number (N), temperature (T), pressure (P), surface elevation (h) of the earth's, phase transition process, and heterogeneous kinetic, that can influence the oxide materials $CaSiO_3$ [68], $MgSiO_3$ [69,70]. In these reports, the researchers found a shift in the number of SiO_x, MgO_y, CaO_z structural units with x, y, z = 4 / 12. However, so far, there have been no specific studies about the structural characteristics of Fe_2O_3 materials at the high temperature (T) the range is 300–7000 K, and high pressure (P) from P = 0 GPa to P = 360 GPa. To elucidate, the phase transition process can be studied based on the change of the number of structural units FeO_4, FeO_5, FeO_6 in the Fe_2O_3 material. In our study are given the results of molecular dynamics simulations to determine the structure, phase transition process of Fe_2O_3 material.

2. Materials and method

Initially, a Fe_2O_3 material with 2000 atoms (800 Fe atoms, 1200 O atoms) was randomly seeded into a model, a cube a nano-size (l), determined by the Eq 1:

$$l = \left(\frac{N}{\rho}\right)^{\frac{1}{3}} = \left(\frac{(2m_{Fe}n_{Fe} + 3m_O n_O)}{\rho}\right)^{\frac{1}{3}} \tag{1}$$

where: $\rho = 5.19$ g/cm^3, and ρ is the specific gravity of Fe_2O_3.

We use this model by the MD simulation method [51,52,71–77] with the force field of the Born-Mayer (BM) pair interaction potential calculated with the Eq 2 [52,58]:

$$U_{ij}(r) = \frac{q_i q_i}{r} + B_{ij}\exp\left(-\frac{r}{R_{ij}}\right) \tag{2}$$

where: q_i, q_j are the charges of ions Fe, O; r is the distance from the ith atom to the jth atom, and B_{ij}, R_{ij} are the parameters chosen as: $B_{Fe-Fe} = 0.0$ eV, $B_{Fe-O} = 2453$ eV, $B_{O-O} = 1500$ eV, $R_{ij} = 29$ pm, $q_{Fe} = +3e$, $q_O = -2e$ [52,58].

To obtain accurate results, we applied periodic boundary conditions to eliminate surface effects.

With the content of the MD method, it is only necessary to determine the interaction between atoms according to the content of Newton's II law. With the interaction of the force field, the atoms will move with the displacement (r) and velocity (v). Within the scope of the content of the article, the interactive force field includes the interaction force field between atoms that obeys Newton's II law and the electronic interaction force field between atoms. To determine the quantities, we use Verlet's algorithm to integrate the equations of motion and are combined them with the average statistical method to determine the energy (E) of each atom, according to the following Eq 3:

$$E = U + K;\ U = \sum_{i>j} U_{ij}(r_{ij})\ ,\ K = \sum_{i=1}^{N} \frac{m_i v_i^2}{2} \tag{3}$$

The rate of increase in temperature (T) and pressure (P) can be calculated with the Eqs 4,5:

$$T(t) = \frac{1}{3Nk_B} \sum_{i=1}^{N} m_i (v_i(t))^2 \tag{4}$$

$$P(t) = \frac{N}{V} k_B T(t) + \frac{1}{3V} \sum_{i<j} r_{ij}(t) F_{ij}(t) \tag{5}$$

where: U, K, N, V are the potential energy, kinetic energy, atomic number, material volume, and $k_B = 1.381 \times 10^{-23}$ J/K is the Boltzmann constant.

The heating process of the model is carried out according to the Eq 6 [52,58]:

$$T = T_0 - \gamma t \tag{6}$$

where: γ is the cooling coefficient, $\gamma = 4.357 \times 10^{13}$ Ks^{-1}.

Initially, it was considered the Fe_2O_3 material model at a temperature (T), T = 7000 K, and it was run 4×10^4 steps of NVT, with NVP recovery statistics (N is the atomic number, V is volume, T is temperature, and pressure P is constant). The simulation was made for each time step of 0.5 fs so that the model discards the initial configuration and stabilizes at the desired temperature (T), and

pressure (P). Then, it was decreased T from T = 7000 K to T = 300 K with a heating rate of dT = 5 K/fs to convert the material model to an amorphous state. This process was followed by an increasing of the temperature T from T = 300 K to T = 900, 1300, 1900, 2300, 2900, 3400, 4500, 5700, 7000 K at P = 0 GPa. Similarly, at T = 300, 2300, 4500, 7000 K, it was increased the pressure P from P = 0 GPa to P = 50, 150, 250, 360 GPa with a turbocharge rate dP = 0.001 GPa/fs with 4×10^4 regression steps that fits all models. After it was obtained the equilibrium in these models, was applied for all models simultaneously running with 10^7 NVE steps (N is the number of atoms, V is the volume, and E is the energy-being constant). The structural results of the models were determined by an average process after 100 simulation steps. During the computation, for all models, the same conditions (N, V, T, P, and E constant) were applied. To study the structure, phase transition process, and heterogeneous kinetics, data analysis, and visualization methods were used. With the obtained results, the structural features were investigated through the radial distribution function (RDF) with the Eq 7 [68–70]:

$$g(r) = \frac{V}{N^2} \left\langle \frac{\sum_i n_i(r)}{4\pi r^2 \Delta r} \right\rangle \tag{7}$$

where: r, $n_i(r)$, V, N, g(r) are the distance between atoms, the density of atoms, volume, number of atoms, and probability of finding an atom between r to r + Δr.

In addition, there are other quantities such as nano-size (1), angular distribution, and average coordination number (CN) that are calculated using the following Eq 8 [68–70]:

$$CN = 4\pi\rho \int_0^{r_1} g(r) r^2 dr \tag{8}$$

where: r_1 is the first peak position of the RDF, and the phase transition temperature (T_m) is determined through the relationship between E and T.

For the bond angle, the relationship between the Fe–O–Fe and O–Fe–O bond angle is used for the link lengths (applied for the links O–O, Fe–O, Fe–Fe), which are determined by the Eq 9:

$$\cos \alpha = \frac{2r_{Fe-O}^2 - r_{Fe-Fe}^2}{2r_{Fe-O}^2} \tag{9}$$

where: α = Fe–O–Fe or O–Fe–O for the model defined at T and P. During heating and pressure, the model annealing is determined by the Nosé-Hoover formula [78,79]. To confirm the accuracy of the results, it was compared our results with those obtained previously under the same T and P conditions. All these results were written in the C programming language and were computed on the computer central system of the Institute of Physics, the Department of Physics and Astronomy of Zielona Gora University, Poland.

3. Results and discussion

3.1. The effect of temperature

To study the structure, and phase transition process of Fe_2O_3 materials with atomic number (N), N = 2000 atoms at temperature (T), T = 300, 900, 1300, 1900, 2300, 3400, 4500, 5700, 7000 K at

pressure (P), P = 0 GPa has applied the simulation method of molecular dynamics (MD) with pair interaction potential Born-Mayer (BM) and conditions periodic boundary, according to Eq 2. The results of the shape, nano-size (l), energy (E) of the system, and radial distribution function (RDF) of links Fe–Fe, Fe–O, O–O pairs are different according to Eq 7 (Figure 1, and Table 1).
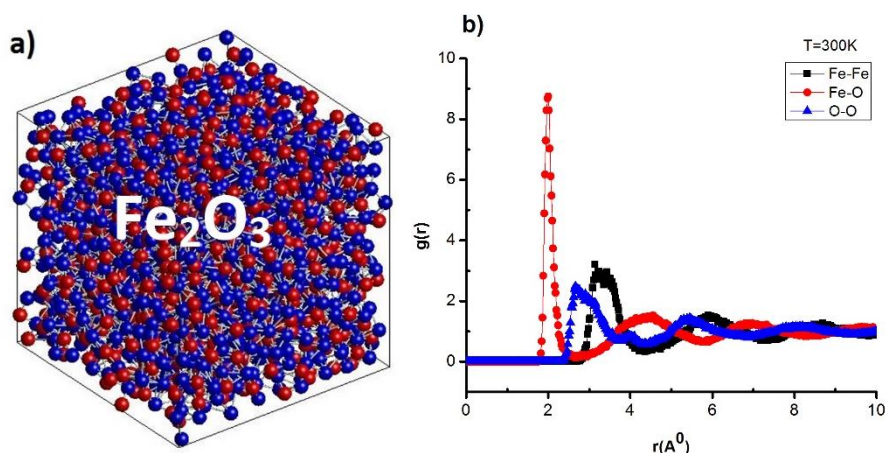
Figure 1. The shape (Fe is red, O is blue) (a), the radial distribution function (b) of materials Fe_2O_3 material at temperature T = 300 K, pressure P = 0 GPa.

Table 1. The structural characteristics of materials Fe_2O_3 material at different temperatures with the pressure P = 0 GPa.

T(K)	r_{ij}(Å)			$g_{ij}(r)$			l (nm)	E (eV)
	Fe–Fe	Fe–O	O–O	Fe–Fe	Fe–O	O–O		
300	3.14	2.00	2.66	3.20	8.75	2.49	2.92	−29.56
900	3.24	1.98	2.72	2.88	7.23	2.28	2.926	−29.40
1300	3.32	1.98	2.78	2.83	6.53	2.30	2.932	−29.29
1900	3.32	1.98	2.82	2.73	5.87	2.23	2.946	−29.13
2300	3.32	1.96	2.84	2.72	5.44	2.20	2.936	−29.01
3400	3.36	1.96	2.86	2.57	4.73	2.05	2.98	−28.67
4500	3.40	1.92	2.94	2.40	4.56	1.88	3.05	−28.24
5700	3.42	1.94	2.92	2.22	4.26	1.79	3.10	−27.86
7000	3.46	1.88	2.96	2.09	4.18	1.71	3.19	−27.41
previous results	3.35 [33,34,53]; 3.11 [33,55,58]; 3.1 [52]	1.91/1.95 [33,34,53]; 2.08 [54]; 1.925/1.945 [33,53]; 1.9 [33,42,52,55,58]	2.91 [34,33,53]; 2.7 [33,42,52,55,58]					

The results show that the Fe_2O_3 material at T = 300 K, P = 0 GPa has a cubic shape, nano-size (l), l = 2.92 nm, the energy (E), E = −29.56 eV and it is generated by two atoms Fe and O (Fe in red, O in blue) (Figure 1a). In addition, the Fe_2O_3 material is made by links Fe–Fe, Fe–O, O–O with the corresponding links lengths $r_{Fe–Fe}$ = 3.14 Å, $r_{Fe–O}$ = 2.00 Å, $r_{O–O}$ = 2.66 Å (Figure 1b). In this case, the obtained results are completely consistent with experimental results with $r_{Fe–Fe}$ = 3.35 Å, $r_{Fe–O}$ = 1.93 Å, $r_{O–O}$ = 2.91 Å [34] and $r_{Fe–Fe}$ = 3.35 Å, $r_{Fe–O}$ = 1.91/1.95 Å, $r_{O–O}$ = 2.91 Å [33,53] and $r_{Fe–O}$ = 2.08 Å [54]; whereas the simulation results with $r_{Fe–Fe}$ = 3.11 Å, $r_{Fe–O}$ = 1.90 Å, $r_{O–O}$ = 2.70 Å [33,55,58] and $r_{Fe–Fe}$ = 3.1 Å, $r_{Fe–O}$ = 1.9 Å, $r_{O–O}$ = 2.7 Å [52]. It can be noted that the link length of bulk materials is always larger than the link length of nanomaterials with nanomaterials is $r_{Fe–Fe}$ = 3.10 Å,

$r_{Fe-O} = 1.9$ Å, $r_{O-O} = 2.7$ Å [33,42,52]. The Fe–Fe link length appears a Pick separation at the first vertex of the RDF into two small peaks, $r_{11} = 3.14$ Å, $r_{12} = 3.4$ Å, which shows that the Fe_2O_3 material, at T = 300 K, exists in the amorphous state, and confirms this result as consistent with previous simulation results [33,34,55]. Besides, the Fe–Fe link length of $r_{11} = 3.11$ Å is related to the number of FeO_4 structural units, whereas $r_{12} = 3.40$ Å is related to the number of FeO_6 structural units and has a common peak [55]. When it is increased the temperature from T = 300 K to T = 900, 1300, 1900, 2300, 3400, 4500, 5700, 7000 K, l increases from l = 2.92 nm to l = 2.926, 2.932, 2.946, 2.936, 2.98, 3.05, 3.10, 3.19 nm altitude and the energy (E) increases from E = −29.56 eV to E = −29.40, −29.29, −29.13, −29.01, −28.67, −28.24, −27.86, −27.41 eV. It can be seen that the influence of temperature on the link lengths r of Fe–Fe, Fe–O, O–O of Fe_2O_3 bulk is very large as r_{Fe-Fe} and increases from $r_{Fe-Fe} = 3.14$ Å to $r_{Fe-Fe} = 3.24$, 3.32, 3.32, 3.32, 3.36, 3.40, 3.42, 3.46 Å; r_{Fe-O} decreases from $r_{Fe-O} = 2.00$ Å to $r_{Fe-O} = 1.98$, 1.98, 1.98, 1.96, 1.96, 1.92, 1.94, 1.88 Å; r_{O-O} increases from $r_{O-O} = 2.66$ Å to $r_{O-O} = 2.72$, 2.78, 2.82, 2.84, 2.86, 2.94, 2.92, 2.96 Å corresponding to the height of the first peak. Also, the radial distribution function g(r) decreases as g_{Fe-Fe} increases from $g_{Fe-Fe} = 3.20$ to $g_{Fe-Fe} = 2.88$, 2.83, 2.73, 2.72, 2.57, 2.40, 2.22, 2.09; g_{Fe-O} decreases from $g_{Fe-O} = 8.75$ to $g_{Fe-O} = 7.23$, 6.53, 5.87, 5.44, 4.73, 4.56, 4.26, 4.18; g_{O-O} increases from $g_{O-O} = 2.49$ to $g_{O-O} = 2.28$, 2.30, 2.23, 2.20, 2.09, 1.88, 1.79, 1.71 (Table 1). On the other hand, during the study, it was found that in the temperature range from T = 300 K to T = 900, 1900, 2300 K and T = 2300 K to T = 3400, 4500, 5700, 7000 K, the g(r) of Fe–O decreases to the smallest value, showing that the Fe_2O_3 material was a phase transition from the amorphous state to the liquid state. The phase transition of Fe_2O_3 materials is a type 1 phase transition. During the heating process of Fe_2O_3 materials, Eq 6 is always applied and the accuracy is evaluated according to the Nosé-Hoover formula [78,79]. To confirm the influence of temperature on structural change, and heterogeneous kinetics, it was determined the average coordination number (CN) according to the Eq 8, and the energy (E) at high temperature (T) (Table 2).

Table 2. Coordination number (CN) of link Fe–Fe, Fe–O, O–O and the energy (E) with Fe_2O_3 material at different temperatures and P = 0 GPa.

T(K)	CN			
	Fe–Fe	Fe–O	O–Fe	O–O
300	11.20	5.44	3.63	15.95
900	11.42	5.35	3.57	15.90
1300	11.40	5.33	3.55	15.82
1900	11.32	5.29	3.53	15.64
2300	11.67	5.60	3.73	15.93
3400	11.06	5.11	3.41	15.28
4500	11.35	5.34	3.56	14.37
5700	9.63	4.64	3.09	13.78
7000	8.63	4.12	2.75	3.55

The results show that, as the temperature increases, the average coordination number (CN) of the link Fe–Fe changes from $CN_{Fe-Fe} = 11.20$ to $CN_{Fe-Fe} = 11.42$, 11.40, 11.32, 11.67, 11.06, 11.35, 9.67, 8.63; Fe–O changes from $CN_{Fe-O} = 5.44$ to

$CN_{Fe-O} = 5.35, 5.33, 5.29, 5.60, 5.11, 5.34, 4.64, 4.12$; O–Fe changes from $CN_{O-Fe} = 3.63$ to $CN_{O-Fe} = 3.57, 3.55, 3.53, 3.73, 3.41, 3.56, 3.09, 2.75$; O–O changes from $CN_{O-O} = 15.95$ to $CN_{O-O} = 15.90, 15.82, 15.64, 15.93, 15.28, 14.37, 13.78, 3.55$ (Table 2), and the energy (E) increases (Table 1).

In this case, the average coordination number of Fe–O decreases from CN = 5.44 to CN = 5.26; this is the FeO_5 structure of Fe_2O_3 material. When it is increased the temperature from T = 300 K to T = 900, 1900, 2300, 3400, 4500, 5700, 7000 K, the average coordination number (CN), and the bonding density of Fe–O, O–Fe tends to decrease, indicating that the oxide material tends to shift to the liquid state. Based on these results, we can realize that the increase of the temperature leads to an increase in the size (1) and E of the material, which proves that there is a major influence of temperature. With extremes, the distribution number of coordination has the value CN > 5.26 with Fe–O and CN > 3.51 with O–Fe, of which the majority is CN = 5.0 with Fe–O, and at CN = 4.0 with O–Fe. On the other hand, at T = 300 K, the amorphous Fe_2O_3 material has a distorted FeO_6 structure with the average coordination number of the Fe–O pair with CN_{Fe-O} value ≈ 6 and it was considered that these FeO_6 structural units are as structural defects [58]. In addition, to analyze the structure of the Fe_2O_3 material oxide material, it was applied the visualization method to study the number of structural units of the material (Figure 2).
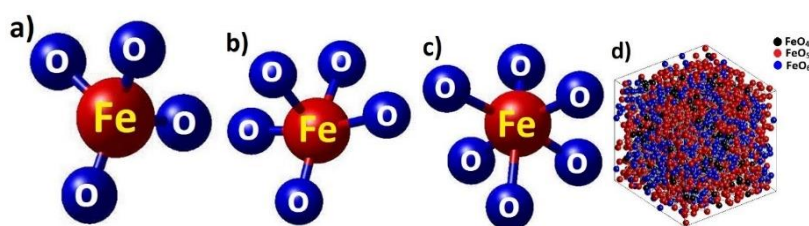
Figure 2: (a) The shape of the number of the structural units Fe_2O_3 material as FeO_4, (b) FeO_5, (c) FeO_6, (d) structure shape at T = 300 K, P = 0 GPa.

The Fe_2O_3 material at T = 300 K, P = 0 GPa exists with 03 structural units: FeO_4 corresponds to one Fe atom link to four O atoms (Figure 2a), similar with FeO_5 (Figure 2b), FeO_6 (Figure 2c), and the structure shape of Fe_2O_3 material with the number of the structural unit of FeO_4 is black, FeO_5 is red, FeO_6 is blue at T = 300 K, P = 0 GPa (Figure 2d). The number of structural units in the Fe_2O_3 material at different temperatures (T) is shown in Table 3.

Table 3. Number of atoms with structural units FeO_4, FeO_5, FeO_6 of Fe_2O_3 material at different temperatures, P = 0 GPa.

Temperature (K)	FeO_4	FeO_5	FeO_6
300	419	1627	1080
900	453	1647	1018
1300	540	1621	1018
1900	676	1640	850
2300	789	1552	833
3400	1175	1501	462
4500	1551	1225	209
5700	1634	1949	201
7000	1634	1049	201

The obtained results show that, when the temperature is increased, the number of structural units FeO_4 increases from 419 to 453, 540, 676, 789, 1175, 1551, 1634, 1634; FeO_5 changes about from 1627 to 1647, 1621, 1640, 1552, 1501, 1225, 1949, 1049; FeO_6 decrease from 1080 to 1018, 1018, 850, 833, 462, 209, 201, 201 (Table 3), showing that the Fe_2O_3 material tends to shift to the liquid state, which demonstrates the influence of temperature on link lengths and the number of structural units that are very big. In addition, the angular distributions of Fe–O–Fe and O–Fe–O are shown in Table 4.

Table 4. The angular distribution of material Fe_2O_3 material at different temperatures.

Temperature (K)	Angular distribution	
	Fe–O–Fe	O–Fe–O
300	105	95
900	105	95
1300	100	95
1900	100	95
2300	100	95
3400	100	95
4500	95	95
5700	95	95
7000	95	95

The obtained results show that, when increasing the temperature, the angle distribution Fe–O–Fe, O–Fe–O between Fe and O atoms has a negligible change around the value of 105° with Fe–O–Fe and with O–Fe–O is 95°. When it is increased the temperature from T = 300 K to T = 900, 1900, 2300, 3400, 4500, 5700, 7000 K, Fe–O–Fe decreases from 105° to 95° and O–Fe–O has a constant value is 95° (Table 4). The obtained results are completely consistent with the simulation results [55,58].

For O–Fe–O bond angle nanomaterials, O–Fe–O has major peaks between 99° and 83°. While the ideal uniform octahedral model has a value of 90°, this is considered the ideal tetrahedral value. The value of 109.5°, confirms the reason that there is a moving to the liquid state, and there are structural units of FeO_5.

The results show that the bond angle O–Fe–O reduced from 105° to 90° when the material changes to the liquid state. These results raise the question of whether the bond angle depends on the length of the links. Through the computational process, was applied the Eq 9, and it was highlighted when $r_{Fe–Fe}$, $r_{O–O}$ increases, $r_{Fe–O}$ decreases. Besides, there is a relationship between the temperature (T) and the energy (E), (Figure 3).
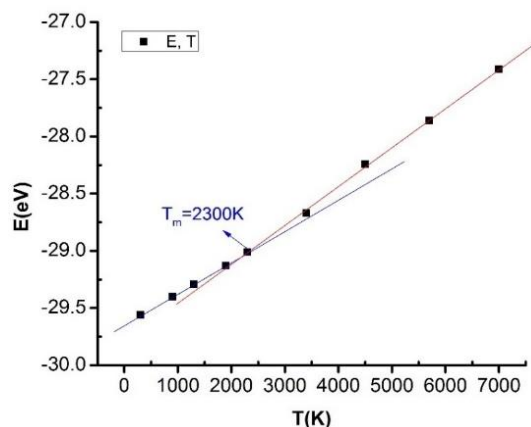
Figure 3. Phase transition temperatures of material Fe_2O_3 material at P = 0 GPa, with different temperatures.

The results show that, when it is increased the temperature (T), form 300–2300 K to 2300–7000 K, the energy (E) of Fe_2O_3 material increases from E = −29.56 eV to E = −29.00 eV and from E = −29.00 eV to E = −27.41 eV. When T increases, T = 300–2300 K then E increases slowly, and between T = 2300 K to T = 7000 K this leads to an E rapid increase. These results show that from T = 300 K to T = 2300 K the Fe_2O_3 material exists in an amorphous state, and E increases slowly. When there is the Fe_2O_3 material at state liquid, E increases rapidly, due to the intersection between the fast-rising energy region and the slowly increasing energy region of 2300 K and calling this is as a point of the phase transition or phase transition temperature (T_m), T_m = 2300 K, corresponding to E = −29.00 eV (Figure 3). This leads to an abrupt change in the density of atoms. When it is increased T, this leads to an increase in nano-size (1), E increases, and the results are like those in simulations of $CaSiO_3$ [68], $MgSiO_3$ [69,70] materials.

The phase transition temperature is one of the most important parameters of amorphous materials, and only the glass temperature (T_g) of Fe_2O_3 nanomaterials was found in the scientific literature [52]. The obtained results show that T_g depends greatly on the nanoparticle nano-size. When it is increased the nano-size (D) of nanomaterials is D = 2–5 nm, the T_g decreases T_g = 2182–1610 K. These results appear to be incomplete in contradiction to previously published bulk materials. In addition, the characteristics of the phase transition from the liquid state to the crystalline state are still unclear with the statements for previously published papers [65,66]. With the phase transition temperature T_m, there is a lack of consensus on studying the nature of the phase transition [63,64,67]. The obtained results show that there is a great influence of temperature on the structure, phase transition process of Fe_2O_3 material.

3.2. Influence of pressure

Similarly, it was studied the effect of pressure (P), P = 0, 50, 150, 250, 360 GPa at temperature (T), T = 300, 2300, 4500, 7000 K, to elucidate the structure, phase transition process of Fe_2O_3 material.

3.2.1. Influence of pressure at temperature 300 K

The Fe_2O_3 material at T = 300 K, leads to an P increasing from P = 0 GPa to P = 50, 150, 250, 360 GPa with structural characteristic results (Figure 4).
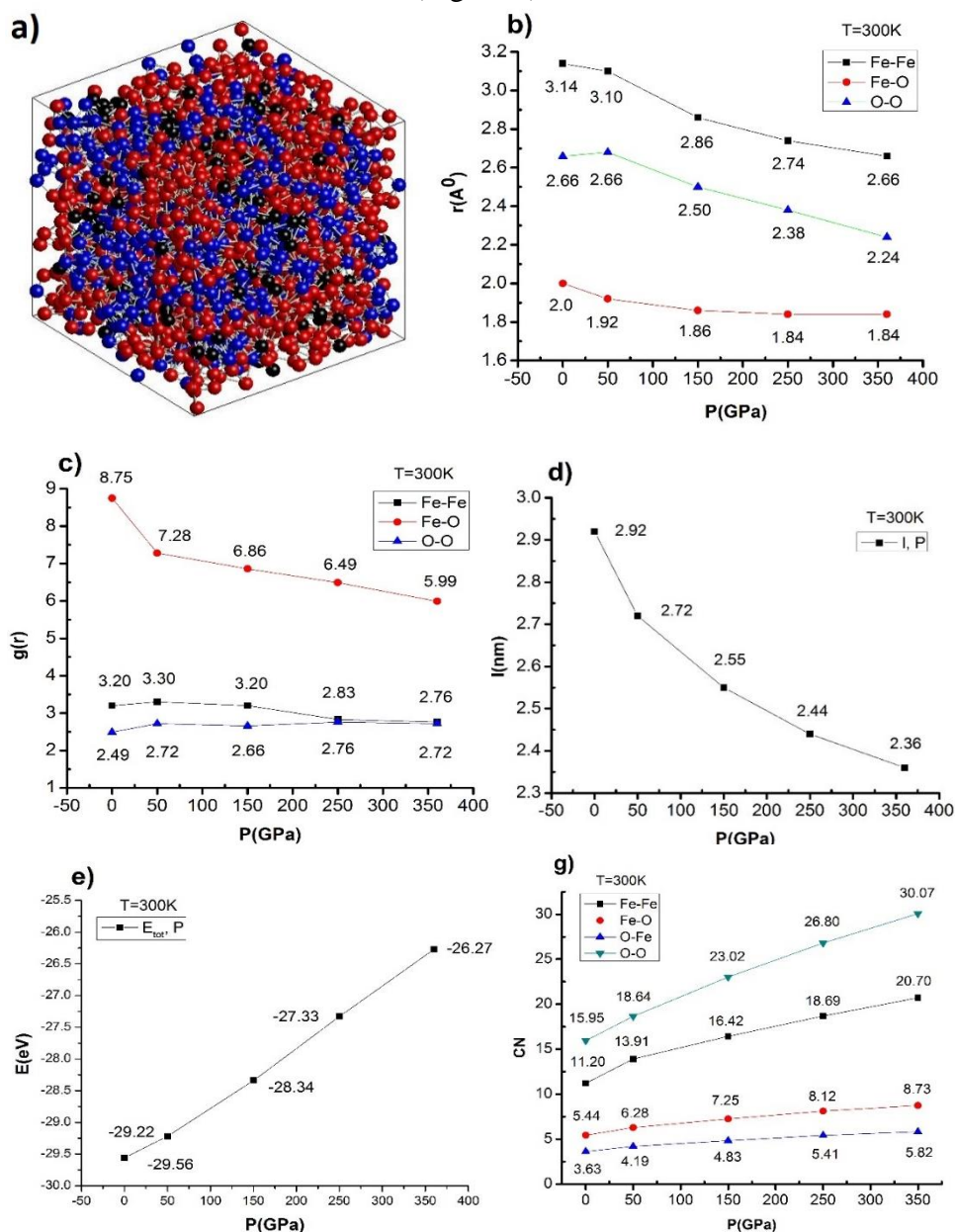
Figure 4. (a) Structural features of material Fe_2O_3 material as structure shape; the links Fe–Fe, Fe–O, O–O of (b) r, (c) g(r); Fe–Fe, Fe–O, O–Fe, O–O at T = 300 K, different P, (d) 1, (e) E, (g) different P.

The results show for the material Fe_2O_3 material at T = 300 K, P = 0 GPa, that it has a structure shape (Figure 4a) and the Fe–Fe, Fe–O, O–O bonding length of Fe–Fe is $r_{Fe–Fe}$ = 3.14 Å, $r_{Fe–O}$ = 2.0 Å, $r_{O–O}$ = 2.66 Å.

Also, the first peak height of the radial distribution function (RDF) of the links is $g_{Fe–Fe}$ = 3.20, $g_{Fe–O}$ = 8.75, $g_{O–O}$ = 2.49. When it is increased P from P = 0 GPa to P = 50, 150, 250, 360 GPa, then

$r_{Fe–Fe}$ decreases from $r_{Fe–Fe} = 3.14$ Å to $r_{Fe–Fe} = 3.10, 2.86, 2.74, 2.66$ Å, and $g_{Fe–Fe}$ increases, and decreases from $g_{Fe–Fe} = 3.20$ to $g_{Fe–Fe} = 3.30, 3.20, 2.83, 2.76$; $r_{Fe–O}$ decreases from $r_{Fe–O} = 2.0$ Å to $r_{Fe–O} = 1.92, 1.86, 1.84, 1.84$ Å, and $g_{Fe–O}$ decreases from $g_{Fe–O} = 8.75$ to $g_{Fe–O} = 7.28, 6.86, 6.49, 5.99$; $r_{O–O}$ decreases from $r_{O–O} = 2.66$ Å to $r_{O–O} = 2.66, 2.50, 2.38, 2.24$ Å, and $g_{O–O}$ changes from $g_{O–O} = 2.49$ to $g_{O–O} = 2.72, 2.66, 2,76, 2.72$ (Figure 4b,c); size (1), decreases from $1 = 2.92$ nm to $1 = 2.72, 2.55, 2.44, 2.36$ nm (Figure 4d), the energy (E) increases from $E = –29.56$ eV to $E = –29.22$, $–28.34, –27.33, –26.27$ eV (Figure 4e) corresponding to the mean coordinate number (CN), $CN_{Fe–Fe}$ increases from $CN_{Fe–Fe} = 11.20$ to $CN_{Fe–Fe} = 13.91, 16.42, 18.69, 20.70$; $CN_{Fe–O}$ increases from $CN_{Fe–Fe} = 5.44$ to $CN_{Fe–Fe} = 6.28, 7.25, 8.12, 8.73$; $CN_{O–Fe}$ increases from $CN_{Fe–Fe} = 3.63$ to $CN_{Fe–Fe} = 4.19, 4.83, 5.41, 5.82$; $CN_{O–O}$ increases from $CN_{Fe–Fe} = 15.95$ to $CN_{Fe–Fe} = 18.64, 23.02, 26.80, 30.07$ (Figure 4g). In addition, the bonding angle of Fe–O–Fe, O–Fe–O and the number of structural units FeO_4, FeO_5, FeO_6 are determined by Figure 5.
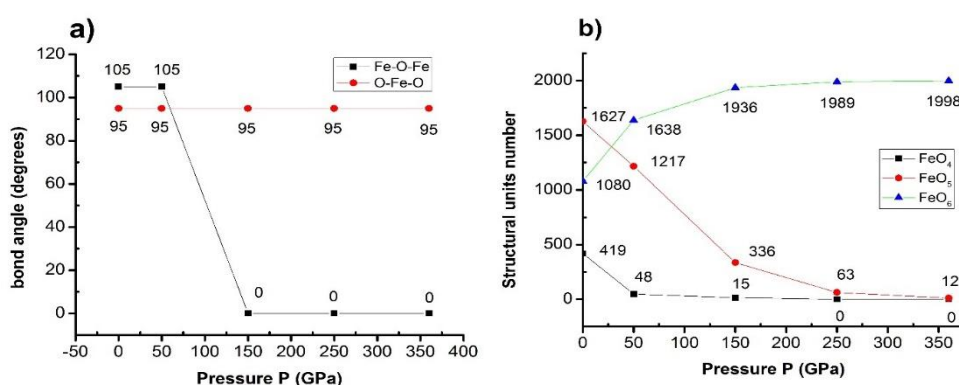
Figure 5. (a) The angular distribution, the number of atoms with structural units FeO_4, FeO_5, (b) FeO_6, of Fe_2O_3 material at T = 300 K with different pressure.

The results show at P = 0 GPa that the angle of Fe–O–Fe is 105°, and of O–Fe–O is 95° corresponding to the number of structural units FeO_4, FeO_5, FeO_6 is 419, 1627, 1080. When it is increased P from P = 0 GPa to P = 50, 150, 250, 360 GPa, then Fe–O–Fe decreases from 105° to 0°, O–Fe–O is 95° (Figure 5a) and FeO_4, FeO_5 decreases from 419 to 48, 15, 0, 0; FeO_5 decreases from 1627 to 1217, 336, 63, 12; FeO_6 increases from 1080 to 1638, 1936, 1989, 1998 (Figure 5b). The obtained results are completely consistent with the results from the literature [80]. Besides, it also shows that r, g(r) decreases when Fe_2O_3 material is at high pressure and low temperature.

3.2.2 Influence of pressure at temperature T = 2300 K

Similarly, with Fe_2O_3 material at T = 2300 K, when P increases from P = 0 GPa to P = 50, 150, 250, 360 GPa, there are structural characteristic results (Figure 6).
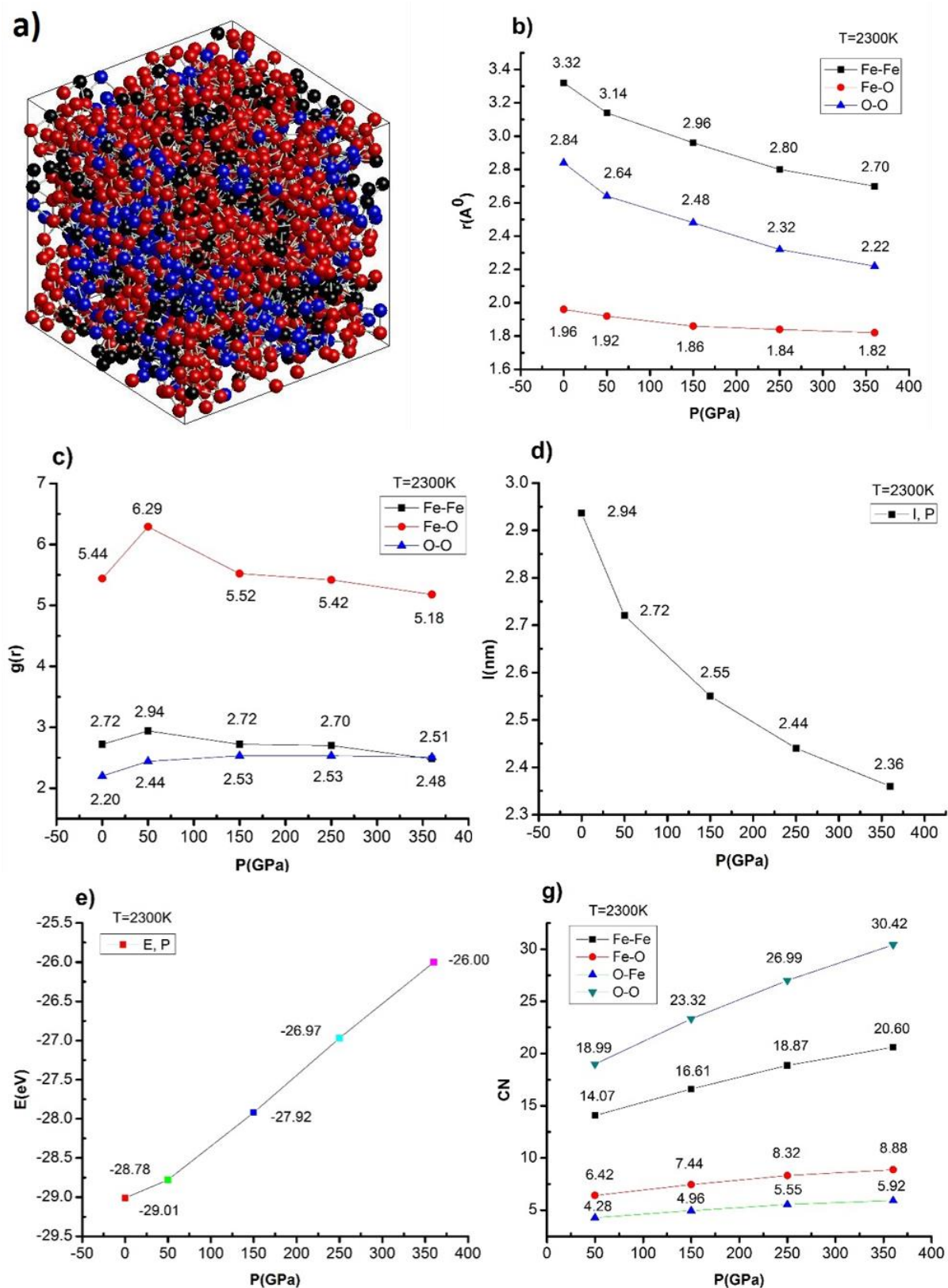
Figure 6. (a) Structural features of material Fe_2O_3 material as structure shape; (b) r, (c) g(r) of the links Fe–Fe, Fe–O, O–O; (d) 1, (e) E, (g) CN of Fe–Fe, Fe–O, O–Fe, O–O at T = 2300 K, different P.

The results show, when Fe_2O_3 material at T = 2300 K, P = 0 GPa, there is a structure shape (Figure 6a), with the length of Fe–Fe, Fe–O, O–O links is 3.32 Å, r_{Fe-O} = 1.96 Å, respectively r_{O-O} = 2.84 Å, the first peak radial distribution function (RDF) of the links is g_{Fe-Fe} = 2.72, g_{Fe-O} = 5.44, g_{O-O} = 2.22 (Figure 6a). When it is increased P from P = 0.0 GPa to P = 50, 150, 250, 360 GPa, r_{Fe-Fe} decreases from r_{Fe-Fe} = 3.32 Å to r_{Fe-Fe} = 3.14, 2.96, 2.80, 2.77 Å, and g_{Fe-Fe} increased, decreases from g_{Fe-Fe} = 2.72 to g_{Fe-Fe} = 2.94, 2.72, 2.70, 2.51; r_{Fe-O} decreases from r_{Fe-O} = 1.96 Å to r_{Fe-O} = 1.92, 1.86, 1.84, 1.82, and g_{Fe-O} increased, decreases from g_{Fe-O} = 5.44 to g_{Fe-O} = 6.29, 5.52, 5.42, 5.18; r_{O-O} decreases from r_{O-O} = 2.84 Å to r_{O-O} = 2.64, 2.48, 2.32, 2.22 Å, and g_{O-O} increased, decreases from g_{O-O} = 2.20 to g_{O-O} = 2.44, 2.53, 2.53, 2.48 (Figure 6b,c); nano-size (1), decreases from 1 = 2.94 nm to 1 = 2.72, 2.55, 2.44, 2.36 nm (Figure 6d) and energy (E) increases from E = −29.01 eV to E = −28.78, −27.92, −26.97, −26.00 eV (Figure 6e) corresponding to the mean coordinate number (CN), CN_{Fe-Fe} increases from CN_{Fe-Fe} = 11.67 to CN_{Fe-Fe} = 14.07, 16.61, 18.87, 20.60; CN_{Fe-O} increases from CN_{Fe-O} = 5.60 to CN_{Fe-O} = 6.42, 7.44, 8.32, 8.88; CN_{O-Fe} increases from CN_{O-Fe} = 3.73 to CN_{O-Fe} = 4.28, 4.96, 5.55, 5.92; CN_{O-O} increases from CN_{O-O} = 15.93 to CN_{O-O} = 18.99, 23.32, 26.99, 30.42; (Figure 6g). The same results are also obtained, with T = 2300 K (Figure 7).
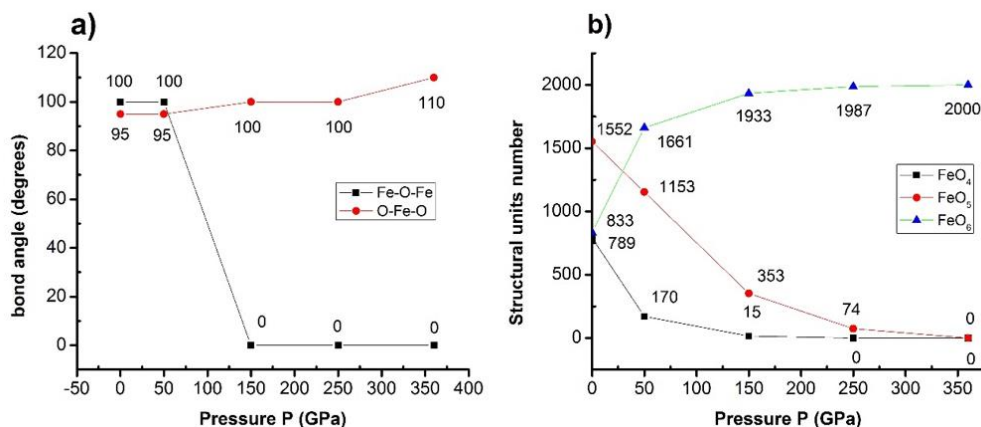
Figure 7. (a) The angular distribution, (b) the number of atoms with structural units FeO_4, FeO_5, FeO_6 of Fe_2O_3 material at T = 2300 K with different pressure.

The obtained results show at P = 0 GPa the bonding angle of Fe–O–Fe is 100°, O–Fe–O is 95° corresponding to the number of structural units (FeO_4, FeO_5, FeO_6 is 789, 1552, 833). When it is increased P from P = 0 GPa to P = 50, 150, 250, 360 GPa, then Fe–O–Fe decreases from 100° to 0°, O–Fe–O increases from 95° to 110° (Figure 7a), and FeO_4 decreases from 789 to 170, 15, 0, 0; FeO_5 decreases 1552 to 1153, 353, 74, 0, and FeO_6 increases from 833 to 1661, 1933, 1987, 2000 (Figure 7b). In it, all r, g(r), 1 decrease and E, CN increase but a smaller decrease at T = 300 K; it shows that in the phase transition temperature T_m = 2300 K, Fe_2O_3 material structure changes to the liquid state, so Fe_2O_3 material structure changes is more stable, when increasing P, it leads to changes in smaller structural features.

3.2.3. Influence of pressure at temperature T = 4500 K

Similarly, when Fe_2O_3 material at T = 4500 K, P is increased from P = 0 GPa to P = 50, 150, 250, 360 GPa there are the structural characteristic results (Figure 8).
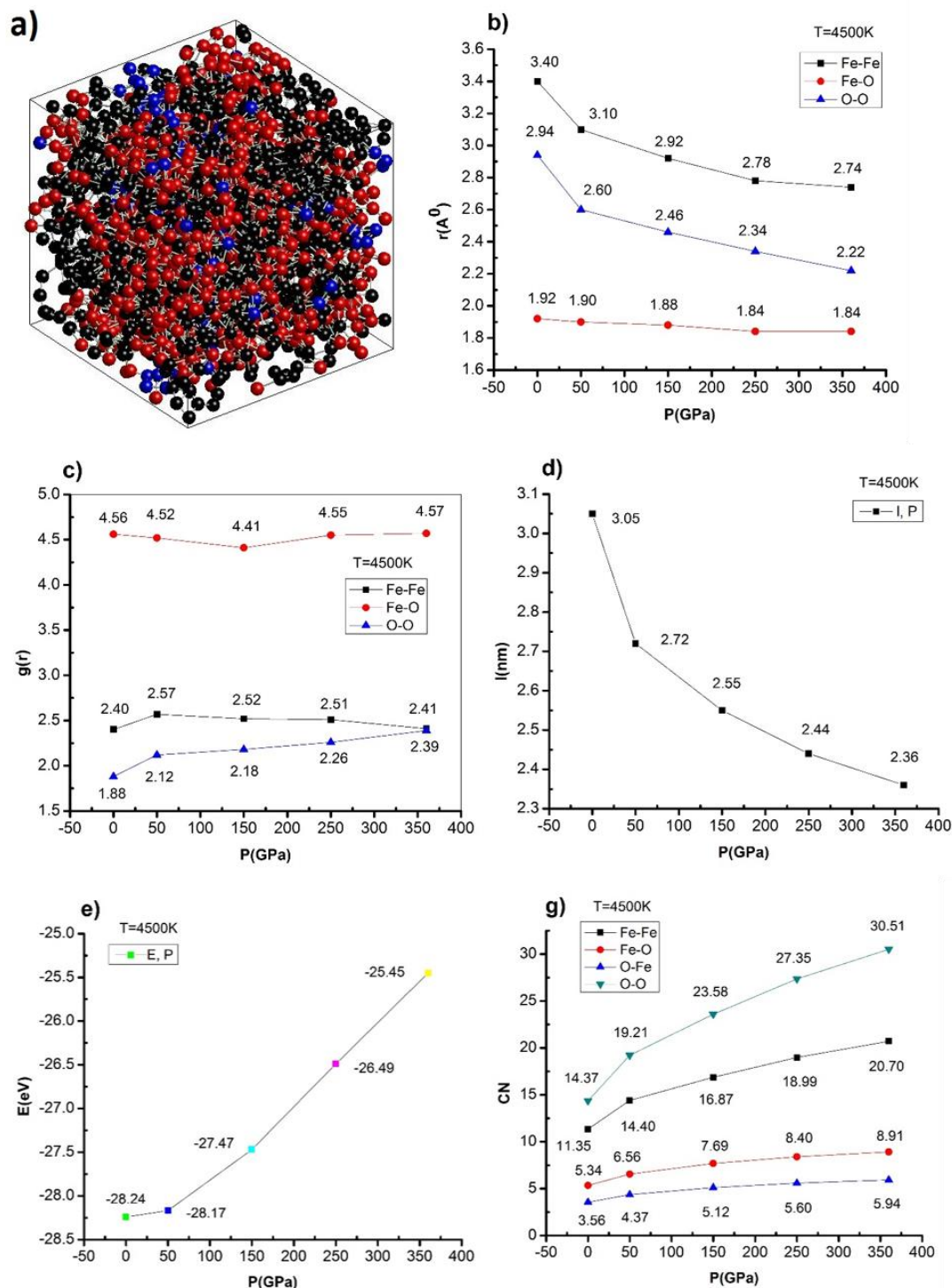
Figure 8. (a) Structural features of material Fe_2O_3 material as structure shape; (b) r, (c) g(r) of the links Fe–Fe, Fe–O, O–O; (d) 1, (e) E, (g) CN of Fe–Fe, Fe–O, O–Fe, O–O at T = 4500 K, different P.

The results show when Fe_2O_3 material at T = 4500 K, P = 0 GPa has a structure shape (Figure 8a), and the length of Fe–Fe, Fe–O, O–O links respectively, r_{Fe-Fe} is 3.40 Å, r_{Fe-O} is 1.92 Å, r_{O-O} is 2.94 Å, the first peak radial distribution function (RDF) of the links is g_{Fe-Fe} = 2.40, g_{Fe-O} = 4.56, g_{O-O} = 1.88. When it is increased P from P = 0 GPa to P = 50, 150, 250, 360 GPa, then r_{Fe-Fe} decreases from r_{Fe-Fe} = 3.40 Å to r_{Fe-Fe} = 3.10, 2.92, 2.78, 2.74 Å, and g_{Fe-Fe} increased, decreases from g_{Fe-Fe} = 2.40 down to g_{Fe-Fe} = 2.57, 2.52, 2.51, 2.41; r_{Fe-O} decreases from r_{Fe-O} = 1.92 Å to r_{Fe-O} = 1.90, 1.88, 1.84, 1.84, and g_{Fe-O} decreases, increased from g_{Fe-O} = 4.56 to g_{Fe-O} = 4.52, 4.41, 4.55, 4.57; r_{O-O} decreases from r_{O-O} = 2.94 Å to r_{O-O} = 2.80, 2.46, 2.34, 2.22 Å, and g_{O-O} increases from g_{O-O} = 1.88 to g_{O-O} = 2.12, 2.18, 2.26, 2.39 (Figure 8b,c); that corresponds to nano-size (1), that decreases from 1 = 3.05 nm to 1 = 2.72, 2.55, 2.44, 2.36 nm (Figure 8d), and energy (E) increases from E = −28.24 eV to E = −28.17, −27.47, −26.49, −25.45 eV (Figure 8e) corresponding to the mean coordinate number (CN); CN_{Fe-Fe} increases from CN_{Fe-Fe} = 11.35 to CN_{Fe-Fe} = 14.40, 16.87, 18.99, 20.70; CN_{Fe-O} increases from CN_{Fe-O} = 5.34 to CN_{Fe-O} = 6.56, 7.69, 8.40, 8.91; CN_{O-Fe} increases from CN_{O-Fe} = 3.56 to CN_{O-Fe} = 4.37, 5.12, 5.60, 5.94; CN_{O-O} increases from CN_{O-O} = 14.37 to CN_{O-O} = 19.21, 23.56, 27.35, 30.51 (Figure 8g). The same results are obtained with T = 4500 K (Figure 9).
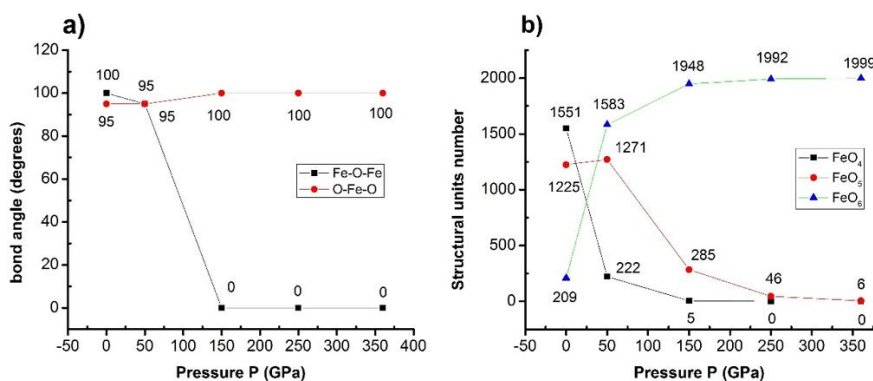
Figure 9. (a) The angular distribution, (b) the number of atoms with structural units FeO_4, FeO_5, FeO_6, of Fe_2O_3 material at T = 4500 K with different pressure.

The obtained results show when P = 0 GPa the bonding angle of Fe–O–Fe is 100°, O–Fe–O is 95° corresponding to the number of structural units FeO_4, FeO_5, FeO_6 is 1551, 1225, 209. When it is increased P from P = 0 GPa to P = 50, 150, 250, 360 GPa, then Fe–O–Fe decreases from 100° to 0°, O–Fe–O increases from 95° to 100° (Figure 9a) and FeO_4 decreases from 1551 to 222, 5, 0, 0; FeO_5 decreases from 1225 to 1271, 285, 46, 6, and FeO_6 increases from 209 to 1583, 1948, 1992, 1999 (Figure 9b).

It can be observed that r, g(r), 1 decrease and E, CN increases, but a smaller decrease at T = 300, 2300 K show that in the high-temperature region, the Fe_2O_3 structure in the liquid state has a smaller structural change.

3.2.4. Influence of pressure at temperature T = 7000 K

Similarly, when Fe_2O_3 material at T = 7000 K, P increased from P = 0 GPa to P = 50, 150, 250, 360 GPa, there are structural characteristic results (Figure 10).
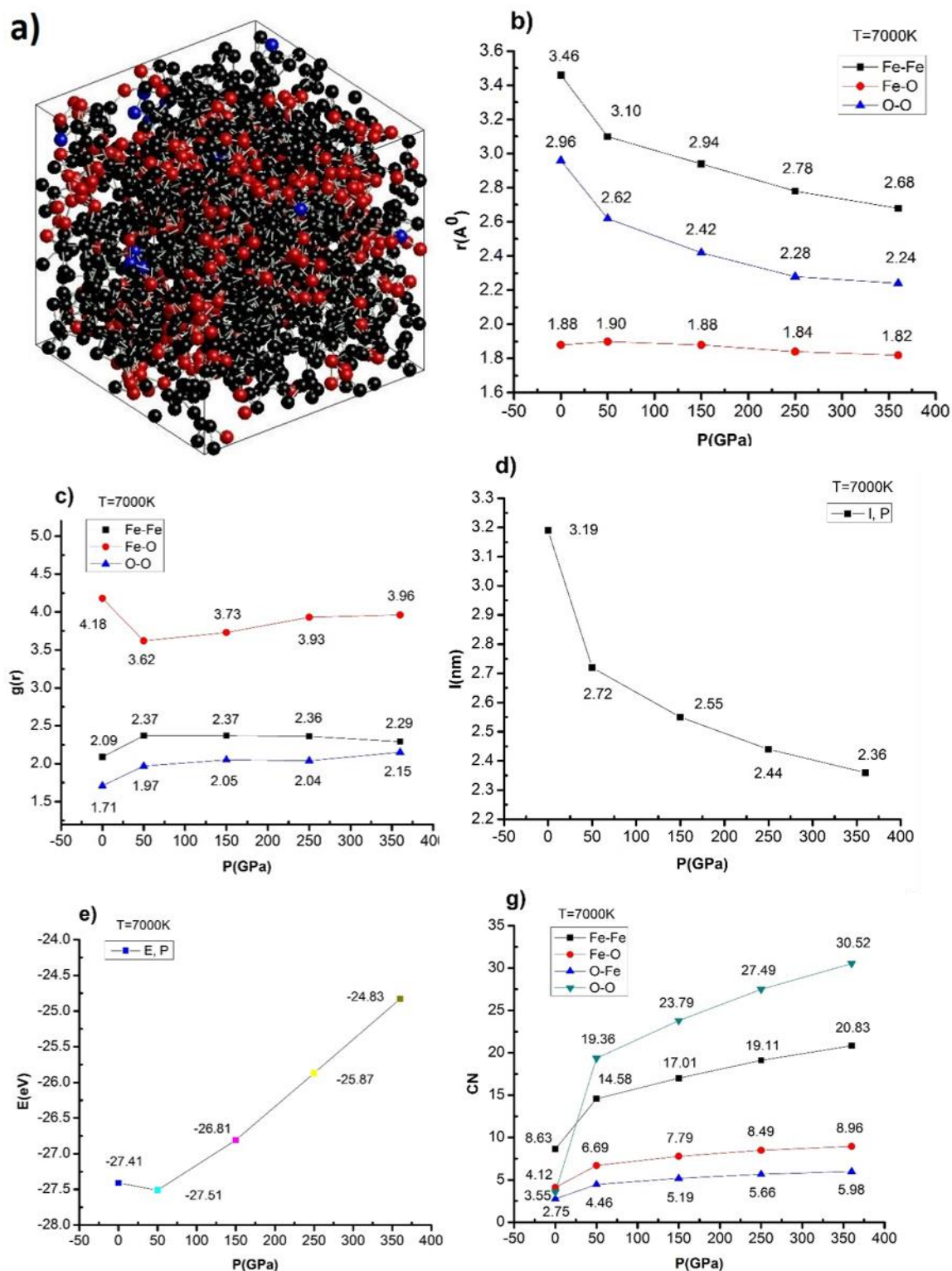
Figure 10. (a) Structural features of material Fe_2O_3 material as structure shape; (b) r, (c) g(r) of the links Fe–Fe, Fe–O, O–O; (d) I, (e) E, (g) CN of Fe–Fe, Fe–O, O–Fe, O–O at T = 7000 K, different P.

The results show when Fe_2O_3 material at T = 7000 K, P = 0 GPa there is a structure shape (Figure 10a) and the length of Fe–Fe, Fe–O, O–O links respectively, $r_{Fe–Fe}$ is 3.46 Å, $r_{Fe–O}$ is 1.88 Å, $r_{O–O}$ is

2.96 Å, the first peak radial distribution function (RDF) of the links is $g_{Fe–Fe} = 2.09$, $g_{Fe–O} = 4.18$, $g_{O–O} = 1.71$. When it is increased P from P = 0 GPa to P = 50, 150, 250, 360 GPa, $r_{Fe–Fe}$ decreases from $r_{Fe–Fe} = 3.46$ Å to $r_{Fe–Fe} = 3.10, 2.94, 2.78, 2.68$ Å, and $g_{Fe–Fe}$ increases, decreases from $g_{Fe–Fe} = 2.09$ to $g_{Fe–Fe} = 2.37, 2.37, 2.36, 2.29$; $r_{Fe–O}$ decreases from $r_{Fe–O} = 1.88$ Å to $r_{Fe–O} = 1.90, 1.88, 1.84, 1.82$ Å, and $g_{Fe–O}$ decreases from $g_{Fe–O} = 4.18$ to $g_{Fe–O} = 3.62, 3.73, 3.93, 3.96$; $r_{O–O}$ decreases from $r_{O–O} = 2.96$ Å to $r_{O–O} = 2.62, 2.42, 2.28, 2.24$ Å, and $g_{O–O}$ increases from $g_{O–O} = 1.71$ to $g_{O–O} = 1.97, 2.05, 2.04, 2.15$ (Figure 10b,c). Also, nano-size (1), decreases from 1 = 3.19 nm to 1 = 2.72, 2.55, 2.44, 2.36 nm (Figure 10d), energy (E) increases from E = −27.41 eV to E = −27.51, −26.81, −25.87, −24.83 eV (Figure 10e), corresponding to the average number of coordinates (CN); $CN_{Fe–Fe}$ increases from $CN_{Fe–Fe} = 8.63$ to $CN_{Fe–Fe} = 14.58, 17.01, 19.11, 20.83$; $CN_{Fe–O}$ increases from $CN_{Fe–O} = 3.55$ to $CN_{Fe–O} = 6.69, 7.79, 8.49, 8.96$; $CN_{O–Fe}$ increases from $CN_{O–Fe} = 2.75$ to $CN_{O–Fe} = 4.46, 5.19, 5.66, 5.98$; $CN_{O–O}$ increases from $CN_{O–O} = 4.12$ to $CN_{O–O} = 19.36, 23.79, 27.79, 30.52$ (Figure 10g). The results are similar with T = 7000 K (Figure 11).
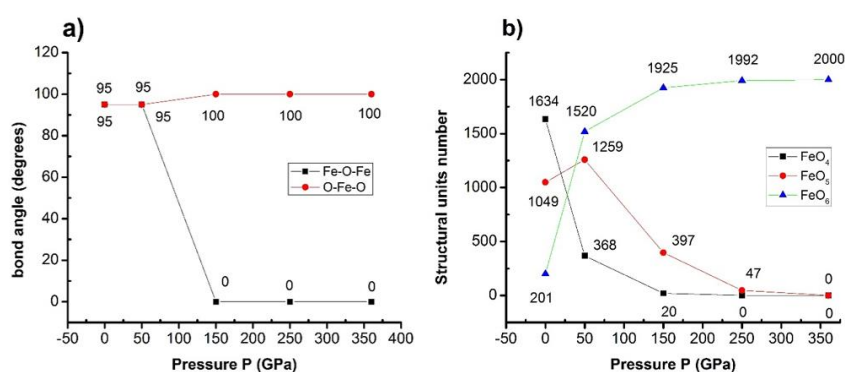
Figure 11. (a) The angular distribution, the number of atoms with structural units FeO_4, (b) FeO_5, FeO_6 of Fe_2O_3 material at T = 7000 K with different pressure.

The obtained results show, at P = 0 GPa the bonding angle of Fe–O–Fe is 95°, O–Fe–O is 95° corresponding to the number of structural units FeO_4, FeO_5, FeO_6 is 1634, 1049, 201. When increasing P from P = 0 GPa to P = 50, 150, 250, 360 GPa then Fe–O–Fe decreases from 95° to 0°, O–Fe–O increases from 95° to 100° (Figure 11a) and FeO_4 decreases from 1634 to 368, 20, 0, 0; FeO_5 changes from 1049 to 1259, 397, 47, 0 and FeO_6 increases from 201 to 1520, 1925, 1992, 2000 (Figure 11b).

In it, all r, g(r), 1 decreases and E, CN increase but with a smaller decrease at T = 2300, 4500 K. All obtained results, when an increase of T = 300–7000 K at P = 0.0 GPa and an increasing of P from P = 0 GPa to P = 50, 150, 250, 360 GPa at T = (300, 2300, 4500, 7000 K) then r, g(r) and 1, E all decrease with T > 4500 K, the decrease led to less, the smallest at T = 7000 K, this result corresponding to CN also increases fewer. In addition, the disappearance in the number of structural units appears with T = 2300 K; with T = 4500 K, FeO_4 disappears at all material with P ≥ 250 GPa and Fe–O–Fe disappears with P ≥ 150 GPa. The obtained results are used as the basis for future experimental results such as determining the link length, and the bonding angle between atoms.

4. Conclusion

The molecular dynamics simulation method has successfully studied the influence of high temperature and high pressure on the structure and phase transition of Fe_2O_3 materials. The results

show that with increasing temperature, the nano-size (1), energy increase, length link decreases, the number of structural units FeO_4, FeO_5 increases, and FeO_6 decreases. In contrast, as pressure increases, then 1 decreases, E increases, FeO_4, FeO_5 decreases, and FeO_6 increases. In addition, when $P \geq 150$ GPa, FeO_4 disappears, FeO_5 disappears at $P \geq 250$ GPa), then only FeO_6 exists at $T = 2300$, 7000 K. It shows that when T increases, FeO_4 increases, FeO_5 increases, FeO_6 decrease when increasing P gives the opposite result. The cause of this phase transition (the phase transition between the amorphous state to the liquid state and from the liquid to the amorphous state) is caused by the nano-size effect. The phase transition follows a type 1 phase transition. With the phase transition, the phase transition temperature (T_m) has been successfully determined, $T_m = 2300$ K, which is the phase transition temperature from the amorphous state to the state. liquid. The obtained results form the basis for future experimental studies.

Conflict of Interest

The authors declare no conflict of interest.

References

1. Zhang L, Hu A (2021) Fe_2O_3 Nanowire flux enabling tungsten inert gas welding of high-manganese steel thick plates with improved mechanical properties. *Appl Sci* 11: 5052. https://doi.org/10.3390/app11115052.
2. Serga V, Burve R, Maiorov M, et al. (2020) Impact of gadolinium on the structure and magnetic properties of nanocrystalline powders of iron oxides produced by the extraction-pyrolytic method. *Materials* 13: 4147. https://doi.org/10.3390/ma13184147
3. Azimov F, Kim J, Choi SM, et al. (2021) Synergistic effects of Fe_2O_3 Nanotube/Polyaniline composites for an electrochemical supercapacitor with enhanced capacitance. *Nanomaterials* 11: 1557. https://doi.org/10.3390/nano11061557
4. Essandoh M, Garcia RA (2018) Efficient removal of dyes from aqueous solutions using a novel hemoglobin/iron oxide composite. *Chemosphere* 206: 502–512. https://doi.org/10.1016/j.chemosphere.2018.04.182
5. Milagres JL, Bellato CR, Ferreira SO, et al. (2020) Preparation and evaluation of hydrocalumite-iron oxide magnetic intercalated with dodecyl sulfate for removal of agrichemicals. *J Environ Manage* 255: 109845. https://doi.org/10.1016/j.jenvman.2019.109845
6. Ge YL, Zhang YF, Yang Y, et al. (2019) Enhanced adsorption and catalytic degradation of organic dyes by nanometer iron oxide anchored to single-wall carbon nanotubes. *Appl Surf Sci* 488: 813–826. https://doi.org/10.1016/j.apsusc.2019.05.221
7. Jin J, Ohkoshi S, Hashimoto K (2004) Giant coercive field of nanometer-sized iron oxide. *Adv Mater* 16: 48–51. https://doi.org/10.1002/adma.200305297
8. Jolivet JP, Tronc E, Chaneac C (2006) Iron oxides: From molecular clusters to solid. A nice example of chemical versatility. *C R Geosci* 338: 488–497. https://doi.org/10.1016/j.crte.2006.04.014
9. Li Y, Zhao L, Wang Y, et al. (2018) Effects of Fe_2O_3 on the properties of ceramics from steel slag. *Int J Miner Metall Mater* 25: 413–419. https://doi.org/10.1007/s12613-018-1586-7
10. Tao S, Liu S, Yuan Y, et al. (2022) A microstructural and compositional study of ε-Fe_2O_3 crystals in the Hare's Fur Jian Ware. *Crystals* 12: 367. https://doi.org/10.3390/cryst12030367

11. Malviya KD, Dotan H, Shlenkevich D, et al. (2016) Systematic comparison of different dopants in thin film hematite (α-Fe$_2$O$_3$) photoanodes for solar water splitting. *J Mater Chem A* 4: 3091–3099. https://doi.org/10.1039/C5TA07095C

12. Xu J, Wen Q, Zhang X, et al. (2021) One-Step construction of multi-walled CNTs loaded with α-Fe$_2$O$_3$ nanoparticles for efficient, photocatalytic properties. *Materials* 14: 2820. https://doi.org/10.3390/ma14112820

13. Sivula K, Formal FL, Gratzel M (2011) Solar water splitting: progress using hematite (α-Fe$_2$O$_3$) photoelectrodes. *Chem Sus Chem* 4: 432–449. https://doi.org/10.1002/cssc.201000416

14. Yu S, Hong VMN, Wang F, et al. (2018) Synthesis and application of iron-based nanomaterials as anodes of lithiumion batteries and supercapacitors. *J Mater Chem A* 6: 9332–9367. https://doi.org/10.1039/C8TA01683F

15. Machala L, Zboril R, Gendanken A (2007) Amorphous iron (III) oxideA review. *J Phys Chem B* 111: 4003–4018. https://doi.org/10.1021/jp064992s

16. Kment S, Riboni F, Pausova S, et al. (2017) Photoanodes based on TiO$_2$ and α-Fe$_2$O$_3$ for solar water splitting–superior role of 1D nanoarchitectures and of combined heterostructures. *Chem Soc Rev* 46: 3716–3769. https://doi.org/10.1039/C6CS00015K

17. Gong XB, You SJ, Wang XH, et al. (2014) A novel stainless steel mesh/cobalt oxide hybrid electrode for efficient catalysis of oxygen reduction in a microbial fuel cell. *Biosens Bioelectron* 55: 237–241. https://doi.org/10.1016/j.bios.2013.12.015

18. Zhu Y, Zhang B, Wang DW, et al. (2015) Order of activity of nitrogen, iron oxide, and FeN$_x$ complexes towards oxygen reduction in alkaline medium. *ChemSusChem* 8: 4016–4021. https://doi.org/10.1002/cssc.201501141

19. Teja AS, Koh PY (2009) Synthesis, properties, and applications of magnetic iron oxide nanoparticles. *Cheminform* 55: 22–45. https://doi.org/10.1002/cssc.201501141

20. Shen S, Lindley SA, Chen X, et al. (2016) Hematite heterostructures for photoelectrochemical water splitting: rational materials design and charge carrier dynamics. *Energy Environ Sci* 9: 2744–2775. https://doi.org/10.1039/C6EE01845A

21. Zhang N, Guo Y, Wang X, et al. (2017) A beta-Fe$_2$O$_3$ nanoparticle-assembled film for photoelectrochemical water splitting. *Dalton Trans* 46: 10673–10677. https://doi.org/10.1039/C7DT00900C

22. Schrebler R, Ballesteros LA, Gomez H, et al. (2014) Electrochemically grown self-organized hematite nanotube arrays for photoelectrochemical water splitting. *J Electrochem Soc* 161: 903–908. https://doi.org/10.1149/2.0481414jes

23. Danno T, Nakatsuka D, Kusano Y, et al. (2013) Crystal structure of β-Fe$_2$O$_3$ and topotactic phase transformation to α-Fe$_2$O$_3$. *Cryst Growth Des* 13: 770–774. https://doi.org/10.1021/cg301493a

24. Zhang N, Wang X, Feng J, et al. (2020) Paving the road toward the use of β-Fe$_2$O$_3$ in solar water splitting: Raman identification, phase transformation and strategies for phase stabilization. *Natl Sci Rev* 7: 1059–1067. https://doi.org/10.1093/nsr/nwaa039

25. Tucek J, Machala L, Ono S, et al. (2015) Zeta-Fe$_2$O$_3$–A new stable polymorph in iron (III) oxide family. *Sci Rep* 5: 15091. https://doi.org/10.1038/srep15091

26. Chirita M, Grozescu I (2009) Fe$_2$O$_3$–Nanoparticles, physical properties and their photochemical and photo electrochemical applications. *Chem Bull* 54: 1–8.

27. Ding Y, Morber JR, Snyder RL, et al. (2007) Nanowire structural evolution from Fe$_3$O$_4$ to ε-Fe$_2$O$_3$. *Adv Funct Matter* 17: 1172–1178. https://doi.org/10.1002/adfm.200601024

28. Yu Q, Meng X, Wang T, et al. (2015) Hematite films decorated with nanostructured ferric oxyhydroxide as photoanodes for efficient and stable photoelectrochemical water splitting. *Adv Funct Mater* 25: 2686–2692. https://doi.org/10.1002/adfm.201500383

29. Tronc E, Chaneac C, Jolivet JP (1998) Structural and magnetic characterization of ε-Fe_2O_3. *J Solid State Chem* 139: 93–104. https://doi.org/10.1006/jssc.1998.7817

30. Yoshikiyo M, Yamada K, Namai A, et al. (2012) Study of the electronic structure and magnetic properties of ε-Fe_2O_3 by first-principles calculation and molecular orbital calculations. *J Phys Chem C* 116: 8688–8691. https://doi.org/10.1021/jp300769z

31. Wang L, Wang Y, Zhang M, et al. (2019) Three-dimensional microstructure of ε-Fe2O3 crystals in ancient chinese sauce glaze porcelain revealed by focused ion beam scanning electron microscopy. *Anal Chem* 91: 13054–13061. https://doi.org/10.1021/acs.analchem.9b03244

32. Yusuf SM, Mukadama MD, Teresa JMD, et al. (2010) Structural and magnetic properties of amorphous iron oxide. *Physica B* 405: 1202–1206. https://doi.org/10.1016/j.physb.2009.11.040

33. Signorini L, Pasquini L, Savini L, et al. (2003) Size-dependent oxidation in iron/iron oxide core-shell nanoparticles. *Phys Rev B* 195423. https://doi.org/10.1103/PhysRevB.68.195423

34. Townsend TK, Sabio EM, Browning ND, et al. (2011) Photocatalytic water oxidation with suspended alpha-Fe_2O_3 particles-effects of nano scaling. *Energy Environ Sci* 4: 4270–4275. https://doi.org/10.1039/C1EE02110A

35. Yen FS, Chen WC, Yang JM, et al. (2002) Crystallite size variations of nano sized Fe_2O_3 powders during γ-to α-phase transformation. *Nano Lett* 2: 245–252. https://doi.org/10.1021/nl010089m

36. Wheeler DA, Wang G, Ling Y, et al. (2012) Nanostructured hematite: synthesis, characterization, charge carrier dynamics, and photoelectrochemical properties. *Energy Environ Sci* 5: 6682–6702. https://doi.org/10.1039/C2EE00001F

37. Machala L, Tucek J, Zboril R (2011) Polymorphous transformations of nanometric iron (III) oxide: A review. *Chem Mater* 23: 3255–3272. https://doi.org/10.1021/cm200397g

38. Tucek J, Zboril R, Namai A, et al. (2010) ε-Fe_2O_3: An advanced nanomaterial exhibiting giant coercive field, millimeter-wave ferromag-netic resonance, and magnetoelectric coupling. *Chem Mater* 22: 6483–6505. https://doi.org/10.1021/cm101967h

39. Yamada K, Tokoro H, Yoshikiyo M, et al. (2012) The phase transition of ε-$In_xFe_{2-x}O_3$ nanomagnets with a large thermal hysteresis loop. *J Appl Phys* 111: 07B506. https://doi.org/10.1063/1.3672075

40. Lindgren T, Wang H, Beermann N, et al. (2002) Aqueous photoelectrochemistry of hematite nanorod array. *Sol Energy Mater Sol Cells* 71: 231–243. https://doi.org/10.1016/S0927-0248(01)00062-9

41. Li Y, Wang Z, Liu R (2021) Superparamagnetic-Fe_2O_3/Fe_3O_4 heterogeneous nanoparticles with enhanced biocompatibility. *Nanomaterials* 11: 834. https://doi.org/10.3390/nano11040834

42. Husain H, Hariyanto B, Sulthonul M, et al. (2018) Local structure examination of mineral-derived Fe_2O_3 powder by Fe K-edge EXAFS and XANES. *IOP Conference Series: Materials Science and Engineering* 367: 012027. https:// doi:10.1088/1757-899X/367/1/012027.

43. Demangeat E, Pédrot M, Dia A, et al. (2018) Colloidal and chemical stabilities of iron oxide nanoparticles in aqueous solutions: the interplay of structural, chemical and environmental drivers. *Environ Sci Nano* 5: 992–1001. https://doi.org/10.1039/C7EN01159H

44. Schaetz A, Reiser O, Stark W (2010) Nanoparticles as semi-heterogeneous catalyst supports. *Chem Eur J* 16: 8950–8967. https://doi.org/10.1002/chem.200903462

45. Vayssieres L, Beermann N, Lindquist SE, et al. (2001) Controlled aqueous chemical growth of oriented three-dimensional crystalline nanorod arrays: application to iron (III) oxides. *Chem Mater* 13: 233–235. https://doi.org/10.1021/cm001202x

46. Beermann N, Vayssieres L, Lindquist SE, et al. (2000) Photoelectrochemical studies of oriented nanorod thin films of hematite. *J Electrochem Soc* 147: 2456–2461. https://doi.org/10.1149/1.1393553

47. Vayssieres L, Sathe C, Butorin SM, et al. (2005) One-dimensional quantum-confinement effect in α-Fe_2O_3 ultrafine nanorod arrays. *Adv Mater* 17: 2320–2323. https://doi.org/10.1002/adma.200500992

48. Erlebach A, Kurland HD, Grabow J, et al. (2015) Structure evolution of nanoparticulate Fe_2O_3. *Nanoscale* 7: 2960–2969. https://doi.org/10.1039/C4NR06989G

49. Touileb K, Hedhibi A, Djoudjou R, et al. (2019) Mixing design for ATIG morphology and microstructure study of 316L stainless steel. *Eng Technol Appl Sci Res* 9: 3990–3997. https://doi.org/10.48084/etasr.2665

50. Chandrasekar G, Kailasanathan C, Vasundara M (2018) Investigation on un-peened and laser shock peened dissimilar weldments of Inconel 600 and AISI 316L fabricated using activated-TIG welding technique. *J Manuf Process* 35: 466–478. https://doi.org/10.1016/j.jmapro.2018.09.004

51. Iglesias O, Labarta A (2001) Finite-size and surface effects in maghemite nanoparticles: Monte Carlo simulations. *Phys Rev B* 63: 184416. https://doi.org/10.1103/PhysRevB.63.184416

52. Hoang VV, Khanh BTHL (2009) Static and thermodynamic properties of liquid and amorphous Fe_2O_3 nanoparticles. *J Phys Condens Matter* 21: 075103. https://doi.org/10.1088/0953-8984/21/7/075103

53. Zhonghua W, Lin G, Qianshu L, et al. (1999) Surface atomic structures of Fe_2O_3 nanoparticles coated with cetyltrimethyl ammonium bromide and sodium dodecyl benzene sulphonate: an extended x-ray absorption fine-structure study. *J Phys Condens Matter* 11: 4961–4970. https://doi.org/10.1088/0953-8984/11/26/301

54. Chen LX, Liu T, Thurnauer MC, et al. (2002) Fe_2O_3 nanoparticle structures investigated by x-ray absorption near-edge structure, surface modifications, and model calculations. *J Phys Chem B* 106: 8539–8546. https://doi.org/10.1021/jp025544x

55. Khanh BTHL, Hoang VV, Zung H (2008) Structural properties of amorphous Fe_2O_3 nanoparticles. *Eur Phys J D* 49: 325–332. https://doi.org/10.1140/epjd/e2008-00168-1

56. Kelm K, Mader W (2005) Synthesis and structural analysis of ε-Fe_2O_3. *Z Anorg Allg Chem* 631: 2383–2389. https://doi.org/10.1002/zaac.200500283

57. Lee S, Xu H (2016) Size-dependent phase map and phase transformation kinetics for nanometric iron (III) oxides ($\gamma \rightarrow \varepsilon \rightarrow \alpha$ pathway). *J Phys Chem* 120: 13316–13322. https://doi.org/10.1021/acs.jpcc.6b05287

58. Belashchenko DK (1997) Computer simulation of the structure and properties of non-crystalline oxides. *Russ Chem Rev* 66: 733–762. https://doi.org/10.1070/RC1997v066n09ABEH000236

59. Mahmoudi M, Stroeve P, Milani AS, et al. (2011) *Superparamagnetic Iron Oxide Nanoparticles: Synthesis, Surface Engineering, Cytotoxicity and Biomedical Applications*, New York: Nova Science Publishers.

60. Muñoz JLG, Romaguera A, Fauth F, et al. (2017) Unveiling a new high-temperature ordered magnetic phase in ε-Fe_2O_3. *Chem Mater* 29: 9705–9713. https://doi.org/10.1021/acs.chemmater.7b03417

61. Dejoie C, Sciau P, Li W, et al. (2014) Learning from the past: rare ε-Fe_2O_3 in the ancient black-glazed Jian (Tenmoku) wares. *Sci Rep* 4: 4941. https://doi.org/10.1038/srep04941

62. Xu H, Lee S, Xu H (2017) Luogufe ngite: a new nano-mineral of Fe_2O_3 polymorph with giant coercive field. *Am Mineral* 102: 711–719. https://doi.org/10.2138/am-2017-5849

63. Wang X, Zhou W (2002) Glass transition of microtome-sliced thin films. *Macromolecules* 35: 6747–6750. https://doi.org/10.1021/ma020291r

64. Schuller J, Melnichenko YB, Richert R, et al. (1994) Dielectric studies of the glass transition in porous media. *Phys Rev Lett* 73: 2224–2228. https://doi.org/10.1103/PhysRevLett.73.2224

65. Zhang Z, Zhao M, Jiang Q (2001) Glass transition thermodynamics of organic nanoparticles. *Physica B* 293: 232–236. https://doi.org/10.1016/S0921-4526(00)00564-0

66. Alcoutlabi M, McKenna GB (2005) Effects of confinement on material behavior at the nanometre size scale. *J Phys Condens Matter* 17: 461–524. https://doi.org/10.1088/0953-8984/17/15/R01

67. Jackson CL, McKenna GB (1996) Vitrification and crystallization of organic liquids confined to nanoscale pores. *Chem Mater* 8: 2128–2137. https://doi.org/10.1021/cm9601188

68. Dung NT (2020) Factors affecting the earth's surface on heterogeneous dynamics of $CaSiO_3$ material. *Mater Sci Eng B* 260: 114648. https://doi.org/10.1016/j.mseb.2020.114648

69. Tuan TQ, Dung NT (2019) Molecular dynamics studies the effects of the earth's surface depth on the heterogeneous kinetics of $MgSiO_3$. *Results Phys* 15: 102671. https://doi.org/10.1016/j.rinp.2019.102671

70. Dung NT, Cuong NC, Van DQ (2019) Molecular dynamics studies the effect of structure $MgSiO_3$ bulk on formation process geology of the Earth. *Int J Comput Mater Sci Eng* 8: 1950011. https://doi.org/10.1142/S2047684119500118

71. Zarringhalam M, Ahmadi-Danesh-Ashtiani H, Toghraie D, et al. (2019) The effects of suspending copper nanoparticles into argon base fluid inside a microchannel under boiling flow condition by using of molecular dynamic simulation. *J Mol Liq* 293: 111474. https://doi.org/10.1016/j.molliq.2019.111474

72. Javadzadegan A, Joshaghani M, Moshfegh A, et al. (2020) Accurate meso-scale simulation of mixed convective heat transfer in a porous media for a vented square with hot elliptic obstacle: an LBM approach. *Physica A* 537: 122439. https://doi.org/10.1016/j.physa.2019.122439

73. Hadipeykani M, Aghadavoudi F, Toghraie D (2020) A molecular dynamics simulation of the glass transition temperature and volumetric thermal expansion coefficient of thermoset polymer based epoxy nanocomposite reinforced by CNT: a statistical study. *Physica A* 546: 123995. https://doi.org/10.1016/j.physa.2019.123995

74. Dung NT, Van CL, Tălu S (2022) Molecular dynamics simulation of bulk Cu material under various factors. *Appl Sci* 12: 4437. https://doi.org/ 10.3390/app12094437.

75. Koparde VN, Cummings PT (2005) Molecular dynamics simulation of titanium dioxide nanoparticle sintering. *J Phys Chem B* 109: 24280–24287. https://doi.org/10.1021/jp054667p

76. Song P, Wen D (2010) Molecular dynamics simulation of the sintering of metallic nanoparticles, *J Nanopart Res* 12: 823–829. https://doi.org/10.1007/s11051-009-9718-7

77. Harris RA (2019) Chemotherapy drug temozolomide adsorbed onto iron-oxide (Fe_3O_4) nanoparticles as nanocarrier: A simulation study. *J Mol Liq* 288: 111084. https://doi.org/10.1016/j.molliq.2019.111084

78. McWilliams RS, Dylan KS, Jon HE, et al. (2012) Phase transformations and metallization of magnesium oxide at high pressure and temperature. *Science* 338: 1330–1333. https://doi.org/10.1126/science.1229450

79. Spaulding DK, McWilliams RS, Jeanloz R, et al. (2017) Evidence for a phase transition in silicate melt at extreme pressure and temperature conditions. *Phys Rev Lett* 108: 065701. https://doi.org/10.1103/PhysRevLett.108.065701

80. Sans JA, Monteseguro V, Garbarino G, et al. (2018) Stability and nature of the volume collapse of ε-Fe_2O_3 under extreme conditions. *Nature communications* 9: 4554. https://doi.org/10.1038/s41467-018-06966-9